

Anisotropy distorts the spreading of a fixed volume porous gravity current

Graham P. Benham¹†

¹Mathematical Institute, University of Oxford, Oxford OX2 6GG, United Kingdom

(Received xx; revised xx; accepted xx)

We consider the release and subsequent gravity-driven spreading of a finite volume of fluid in an anisotropic porous medium bounded by an impermeable substrate. When the permeability in the vertical direction is much smaller than the horizontal direction, as is the case in many real geological reservoirs, this restricts the spread of the current to a very thin layer near the impermeable base. Asymptotic analysis reveals two separate flow regimes. At early times the bulk of the current descends slowly and uniformly, injecting fluid into thin finger-like regions near the base. At much later times the current transitions to the classical gravity-driven solution and continues to spread with a self-similar shape. One interesting consequence is that the swept volume of the current grows differently depending on the anisotropy of the medium. This has important consequences for managing contaminant spills, where it is important to minimise the contacted volume of the aquifer, or during geological CO₂ sequestration where a larger contacted volume results in more CO₂ being stored.

1. Introduction

Gravity-driven flows resulting from the release of a fluid within a porous medium are a common feature of environmental fluid dynamics. For example, such flows arise when groundwater responds to heavy rainfall (Guérin *et al.* 2014), after the spillage of a contaminant (Bear & Cheng 2010), or during the geological storage of carbon dioxide in saline aquifers (Huppert & Neufeld 2014). Since all geological aquifers are heterogeneous and often this heterogeneity manifests as an anisotropic permeability field (Woods 2015), it is important to quantify how this affects the migration speeds and shape of the current. This is particularly relevant to situations where it is desirable to minimise the volume of the aquifer contacted by the fluid (e.g. containing the spread of a contaminant) or to maximise the contacted volume (e.g. trapping residual saturation during CO₂ storage).

In the case of homogeneous and isotropic porous media, there have been numerous studies on the evolution of fixed volume gravity currents. Some of these studies have treated single-phase flows (Huppert & Woods 1995), whilst others have incorporated multiphase effects such as residual trapping (Hesse *et al.* 2008; Golding *et al.* 2017) and dissolution within the ambient fluid (MacMinn *et al.* 2011). In some cases simple scaling laws were derived by exploiting the self-similar properties of gravity currents, as shown by Barenblatt (1952) in the case of single-phase flow, and by Kochina *et al.* (1983) in the case of trapped residual saturation. Later work by Hesse *et al.* (2007) and Ball *et al.* (2017) explored the transition to self-similarity in both confined and unconfined settings. However, in the case where the porous medium is heterogeneous or anisotropic, as is the case for real geological reservoirs, the behaviour of a fixed volume gravity current has not yet been addressed.

† Email address for correspondence: benham@maths.ox.ac.uk

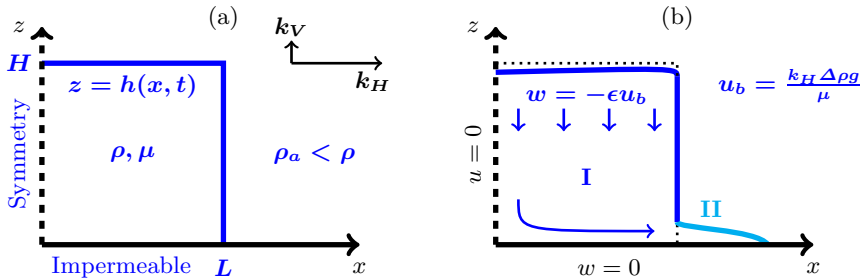


Figure 1: Schematic diagram. (a) A finite volume $2LH\phi$ of dense fluid is released into a porous medium with an anisotropic permeability field $k_H \gg k_V$ above an impermeable base. (b) The medium is initially saturated with a less dense fluid so that the bulk region (I) descends slowly at speed $-\epsilon u_b$, where $\epsilon = k_V/k_H$, whilst a thin finger region (II) develops near the base of the current.

In the case of heterogeneous media some progress has been made for gravity currents resulting from constant injection. For example, Jackson & Krevor (2020) explored how heterogeneities of different lateral and vertical scales affect the migration speed of a CO_2 plume. Likewise, Benham *et al.* (2022) addressed the case of a gravity current resulting from point source injection in an anisotropic medium. In this case, it was shown that anisotropy can cause a build-up of pressure that stretches the flow into an ellipsoid shape during an early-time regime of the flow, before transitioning to a gravity-dominated regime at much later times. However, in the case of a released fixed volume (i.e. in the absence of injection) it is not known how such anisotropy affects the flow development.

Such flows are particularly relevant to the context of CO_2 storage in geological reservoirs as a means to reduce emissions and limit the effects of global warming (Huppert & Neufeld 2014). In such scenarios, buoyant CO_2 is injected into a brine-filled reservoir beneath an impermeable cap rock. Once the injection is switched off, the CO_2 rises and spreads out beneath the cap rock, with a fraction of its mass being lost to residual trapping (via the drainage/imbibition cycle) and dissolution within the surrounding brine (MacMinn *et al.* 2011; Krevor *et al.* 2015). Hence, to quantify the trapping potential of different geological reservoirs (e.g. when choosing potential storage sites) it is important to understand how the anisotropy of the aquifer may affect the historical migration of the current across the pore space of the aquifer.

In this study we demonstrate that anisotropy restricts the flow of the gravity current to thin finger-like regions spreading near the impermeable boundary, qualitatively similar to those predicted by other studies (Jackson & Krevor 2020). Due to this flow distortion, the swept volume of the current is reduced for anisotropic aquifers. This indicates that isotropic aquifers may have better potential for certain forms of trapping that depend on the contacted volume of pore space.

2. Finite release in anisotropic media

We consider an anisotropic porous medium in which the horizontal permeability k_H is much larger than the vertical permeability k_V . Such anisotropic flow properties are a common feature in geological reservoirs and may result from the deposition of successive layers of fine and coarse material or from post-depositional compaction of the formation (Corbett & Jensen 1992). As we will show, the anisotropy of the medium restricts the vertical flow of the bulk of the fluid, which we denote region I (see figure 1), resulting in a

slow migration towards the impermeable boundary. Meanwhile, gravity-driven spreading is limited to thin finger-like regions near the base, which we denote region II .

For simplicity, we restrict our attention to two-dimensional flows and we consider the release of a volume (per unit width) of fluid with constant density ρ . The surrounding porous medium is initially saturated with an ambient fluid with relatively smaller density $\rho_a < \rho$. Due to the Boussinesq approximation (Soltanian *et al.* 2016), these results also apply in the case of a lighter fluid (e.g. CO₂) released within a porous medium saturated with a heavier fluid (e.g. brine), with the impermeable boundary located above rather than below.

For the sake of simplicity we take the viscosity of the released fluid and the ambient fluid to be the same (μ), and we consider that the initial shape of the released fluid is rectangular, with dimensions $2L \times H$ (although these results would apply to any similar convex shape). The flow in the released volume of fluid is subject to the two-dimensional Darcy equations,

$$\mathbf{u} = -\frac{1}{\mu} \underline{\mathbf{k}} \cdot \nabla [p + \rho g z], \quad (2.1)$$

$$\nabla \cdot \mathbf{u} = 0, \quad (2.2)$$

where \mathbf{u} is the Darcy velocity vector, p is the pressure, and $\underline{\mathbf{k}} = \text{diag}(k_H, k_V)$ is the anisotropic permeability field in the x, z directions. Combining (2.1),(2.2), the pressure satisfies Laplace's equation with anisotropic coefficients,

$$\frac{\partial^2 p}{\partial x^2} + \epsilon \frac{\partial^2 p}{\partial z^2} = 0, \quad (2.3)$$

where the anisotropy is given by

$$\epsilon = \frac{k_V}{k_H} \ll 1. \quad (2.4)$$

The boundary conditions for the flow in region I are as follows. The left hand and bottom boundaries, $x = 0$, $z = 0$, are assumed to be symmetric and impermeable, respectively, so we prescribe no normal flow,

$$u = 0 : \quad x = 0, \quad (2.5)$$

$$w = 0 : \quad z = 0. \quad (2.6)$$

Likewise, at the fluid interface, which we denote $z = h(x, t)$, we impose the dynamic and kinematic boundary conditions:

$$p = p_a - \rho_a g h : \quad z = h(x, t), \quad (2.7)$$

$$w = \phi \frac{\partial h}{\partial t} + u \frac{\partial h}{\partial x} : \quad z = h(x, t). \quad (2.8)$$

The former condition matches the pressure in the fluid with the ambient hydrostatic pressure, whilst the latter condition imposes that a particle at the interface remains at the interface (Gilmore *et al.* 2022; Benham 2022).

In the limit $\epsilon \rightarrow 0$, mass conservation (2.2) indicates that if there is no vertical flow (i.e. $k_V = 0$) then there cannot be any horizontal flow either. Essentially, the governing equation (2.3) implies that the pressure (which is continuous) is set by the ambient fluid, such that $p = p_a - \rho_a g z$, and the resulting velocities are $u = w = 0$. Hence, the interface remains at the initial position $z = h_0(x)$ for all time.

Now let's consider the case of a strongly anisotropic porous medium, such that $0 < \epsilon \ll 1$. In this case, the pressure is still hydrostatic (set by the ambient fluid) at leading

order. However, this produces a small but finite vertical velocity within region I, such that

$$w = -\epsilon u_b, \quad (2.9)$$

where $u_b = k_H \Delta \rho g / \mu$ is the buoyancy velocity, written in terms of the density difference $\Delta \rho = \rho - \rho_a$. Since (2.9) does not satisfy the impermeability condition (2.6), a boundary layer must be introduced near $z = 0$. To analyse this boundary layer we convert to a set of stretched dimensionless variables

$$x = L\xi, \quad z = \epsilon^{1/2} L\zeta, \quad p = p_a - \rho_a g z + \epsilon^{1/2} \Delta \rho g L P, \quad (2.10)$$

where ξ , ζ and P are $\mathcal{O}(1)$. In this way, within the boundary layer region the governing equations and boundary conditions (2.3), (2.5) and (2.6) become

$$\frac{\partial^2 P}{\partial \xi^2} + \frac{\partial^2 P}{\partial \zeta^2} = 0, \quad (2.11)$$

$$\frac{\partial P}{\partial \xi} = 0 : \quad \xi = 0, \quad (2.12)$$

$$\frac{\partial P}{\partial \zeta} = -1 : \quad \zeta = 0. \quad (2.13)$$

In addition, we require that the *inner* solution (within the boundary layer) matches with the *outer* solution (far outside the boundary layer), such that

$$P \rightarrow 0 : \quad \zeta \rightarrow \infty. \quad (2.14)$$

The final boundary condition needs more careful thought. Since there is a vertical velocity (2.9) descending through the outer region, this induces an arrival of flux $\epsilon u_b L$ within the inner region. However, since this flux can go neither downwards nor leftwards (due to impermeable/symmetric boundaries), it must instead exit through the right hand boundary $x = L$. In other words, the right hand interface must move outwards to conserve mass, creating a new finger-like region of vertical size $z \sim \mathcal{O}(\epsilon^{1/2})$, which we denote region II. Hence, the final boundary condition for region I is given by an integral constraint of the form

$$\int_0^\infty -\frac{\partial P}{\partial \xi} \Big|_{\xi=1} d\zeta = 1. \quad (2.15)$$

The descent of the upper interface in region I and the resulting finger-like region II are both illustrated in figure 1b.

Before addressing these details further, we first note that (2.11)-(2.15) can be solved exactly by separation of variables. Hence, the composite solution for the inner and outer regions is given by

$$p = p_a - \rho_a g z + 2\epsilon^{1/2} \Delta \rho g L \sum_{n=0}^{\infty} \frac{(-1)^n}{\lambda_n^2} \cos \left[\frac{\lambda_n x}{L} \right] \exp \left[-\frac{\lambda_n z}{\epsilon^{1/2} L} \right], \quad (2.16)$$

where $\lambda_n = (2n + 1)\pi/2$. Conservation of mass within region I indicates that

$$\phi \frac{\partial h}{\partial t} + \frac{k_H}{\mu} \frac{\partial}{\partial x} \left[\int_0^{h(x,t)} -\frac{\partial p}{\partial x} dz \right] = 0. \quad (2.17)$$

Hence, inserting (2.16) into (2.17) results in the governing equation for the evolution of

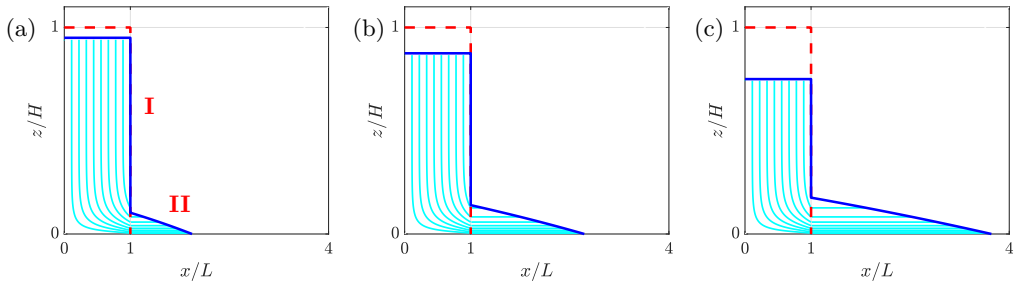


Figure 2: Approximate solutions for regions I and II in the case of $\epsilon = 10^{-2}$. Times are given in terms of the transition time (2.33), where (a) $t/t^* = 0.07$, (b) $t/t^* = 0.17$ and (c) $t/t^* = 0.34$. Streamlines are evaluated using velocities derived from (2.16) and (2.20).

the thickness of the current, which is

$$\phi \frac{\partial h}{\partial t} - u_b \epsilon L \frac{\partial}{\partial x} \sum_{n=0}^{\infty} \frac{2(-1)^{n+1} \sin \lambda_n x/L}{\lambda_n^2} \left(1 - \exp \left[-\frac{\lambda_n h(x, t)}{\epsilon^{1/2} L} \right] \right) = 0. \quad (2.18)$$

This can be further simplified by ignoring exponentially small terms when h/L is larger than $\mathcal{O}(\epsilon^{1/2})$, and by using the fact that the infinite sum converges to $-x/L$. Hence, we see that the height within region I is given by

$$h = H - \frac{\epsilon u_b t}{\phi}, \quad (2.19)$$

which is valid for $0 < x < L$ and for $h \gg \mathcal{O}(\epsilon^{1/2})$.

Next, we address the fluid flow in region II, which is the finger-like region of escaped fluid near the base of the current, which is defined for $L < x < x_N(t)$, where $x_N(t)$ is the maximum extent of the finger. This flow region is long and thin (like a classical gravity current) such that the horizontal velocity is much larger than the vertical velocity. Consequently, the pressure within region II is hydrostatic to good approximation, such that

$$p = p_a - \rho_a g h - \rho g (z - h). \quad (2.20)$$

Similarly to (2.17), conservation of mass within this region gives

$$\phi \frac{\partial h}{\partial t} = u_b \frac{\partial}{\partial x} \left[h \frac{\partial h}{\partial x} \right], \quad (2.21)$$

which is sometimes called the Dupuit approximation. This is accompanied by boundary conditions that correspond with imposing the input flux from region I,

$$-u_b h \frac{\partial h}{\partial x} = \epsilon u_b L : \quad x = L, \quad (2.22)$$

and imposing zero thickness and zero flux at the moving front,

$$h \rightarrow 0 : \quad x \rightarrow x_N(t), \quad (2.23)$$

$$-u_b h \frac{\partial h}{\partial x} \rightarrow 0 : \quad x \rightarrow x_N(t). \quad (2.24)$$

By introducing dimensionless coordinates,

$$h = \epsilon L \mathcal{H}, \quad x = L(\epsilon \xi + 1), \quad t = \frac{\phi \epsilon L}{u_b} \tau, \quad (2.25)$$

we get the same system as Huppert & Woods (1995) for a constant input flux. The solution is well known and is given in terms of the similarity variables

$$\eta = \xi / \tau^{2/3}, \quad \mathcal{H} = \tau^{1/3} f(\eta). \quad (2.26)$$

The self-similar shape function $f(\eta)$ is defined for $\eta \in [0, \eta_N = 1.482]$, and is monotone decreasing from $f_0 := f(0) = 1.296$ to $f(\eta_N) = 0$. The solution for regions I and II is plotted in figure 2a,b,c, at several different times. Streamlines confirm that the flux into region II is fed by the shrinking of region I.

2.1. Transition to self-similarity

After a long time the flow is expected to eventually transition to the self-similar behaviour of a finite release gravity current (Huppert & Woods 1995; Ball *et al.* 2017). As discussed by Benham *et al.* (2022), the late-time dynamics of a two-dimensional gravity current are independent of the anisotropy of the medium since the bulk flow decouples from the ambient. Hence, the anisotropy only affects the late-time behaviour by delaying the time to transition to self-similarity. Hence, to study the late-time behaviour we first analyse the isotropic case, which determines the late-time dynamics, and then use these dynamics to derive the time t^* to transition between the early and late solutions, where t^* depends on the anisotropy ϵ .

As before, the thickness of the gravity current satisfies the Dupuit approximation (2.21). The boundary conditions are similar to the case of constant input flux, as described above, except the left hand boundary condition is replaced with the zero flux condition

$$\frac{\partial h}{\partial x} = 0: \quad x = 0. \quad (2.27)$$

Consequently, mass conservation indicates that

$$\int_0^{x_N(t)} h \, dx = HL. \quad (2.28)$$

By introducing dimensionless coordinates,

$$x = (HL)^{1/2} \xi, \quad h = (HL)^{1/2} \mathcal{H}, \quad t = \frac{\phi (HL)^{1/2}}{u_b} \tau, \quad (2.29)$$

and switching to similarity variables

$$\eta = x / \tau^{1/3}, \quad \mathcal{H} = \tau^{-1/3} f(\eta), \quad (2.30)$$

we arrive at a system of equations that can be solved analytically to give

$$f(\eta) = \frac{1}{6}(\eta_N^2 - \eta^2), \quad (2.31)$$

where $\eta_N = 3^{2/3}$, and this is plotted in (Huppert & Woods 1995).

Next, we discuss the time taken to transition from the early flow regime involving two fluid regions to the late flow regime with a single region which is self-similar. In the early regime the vertical extent of the flow descends according to (2.19). By contrast, the vertical extent of region II ($\epsilon L \mathcal{H}$ in (2.25)) increases like $\sim f_0 (u_b \epsilon^2 L^2 t / \phi)^{1/3}$. Hence, it is

expected that the transition to self-similarity will occur once these two thickness scalings approach each other. Thus, the transition time t^* satisfies the cubic equation

$$\left(H - \frac{\epsilon u_b t^*}{\phi}\right)^3 = \frac{f_0^3 u_b \epsilon^2 L^2 t^*}{\phi}. \quad (2.32)$$

The solution has a complicated form but can be expanded in powers of $\epsilon \ll 1$ to give

$$t^* = \frac{L\phi}{u_b \epsilon} \left[\alpha - f_0 \alpha^{1/3} \epsilon^{1/3} + \frac{f_0^2}{3\alpha^{1/3}} \epsilon^{2/3} + \dots \right], \quad (2.33)$$

where $\alpha = H/L$ is the aspect ratio of the initial current shape. Hence, anisotropy delays the transition to a classical self-similar regime, which is consistent with other studies (Benham *et al.* 2022). At the transition time t^* the maximum thickness of the current (which we denote H^*) is given by

$$H^* = L\epsilon^{1/3} \left[f_0 \alpha^{1/3} - \frac{f_0^2}{3\alpha^{1/3}} \epsilon^{1/3} + \dots \right]. \quad (2.34)$$

This indicates that, by the time transition occurs for very anisotropic media, the bulk of the current has shrunk significantly. This hints towards a reduced swept volume, which we analyse further in the next section.

3. Swept shape and swept volume

As described earlier, it is useful for applications (e.g. contaminant transport or CO₂ storage) to quantify the total volume contacted by the gravity current over all times, also known as the swept volume[†]. At early times $t \ll t^*$ region I shrinks uniformly downwards whilst region II grows upwards and outwards. Hence, the swept volume \mathcal{V} is simply equal to the initial volume plus the instantaneous volume of region II, such that

$$\mathcal{V}(t) = 2HL + 2\epsilon u_b Lt. \quad (3.1)$$

At much later times $t \gg t^*$, once the gravity current has transitioned to self-similarity, the thickness $z = h(x, t)$ has some parts which are growing and other parts which are shrinking, so this requires more careful attention. To deal with this we first define the swept shape \mathcal{S} as the maximum thickness that the current ever reached at a given value of x , such that

$$\mathcal{S}(x) = \max_t \{h(x, t)\}. \quad (3.2)$$

The swept volume is then given in terms of \mathcal{S} as

$$\mathcal{V}(t) = 2 \int_0^{x_N(t)} \mathcal{S} dx. \quad (3.3)$$

The swept shape (3.2) is calculated by finding the time at which the current thickness is maximal, which is equivalent to $\eta = 3^{1/6}$ in the similarity solution f (2.31). Inserting this into (3.2) we get

$$\mathcal{S}(x) = \frac{HL}{3^{1/2}x}, \quad (3.4)$$

[†] Note that since our model is in two dimensions, the swept volume is taken as per unit width. Also note that the total volume of fluid is constant and given by $2HL\phi = \phi\mathcal{V}(0)$.

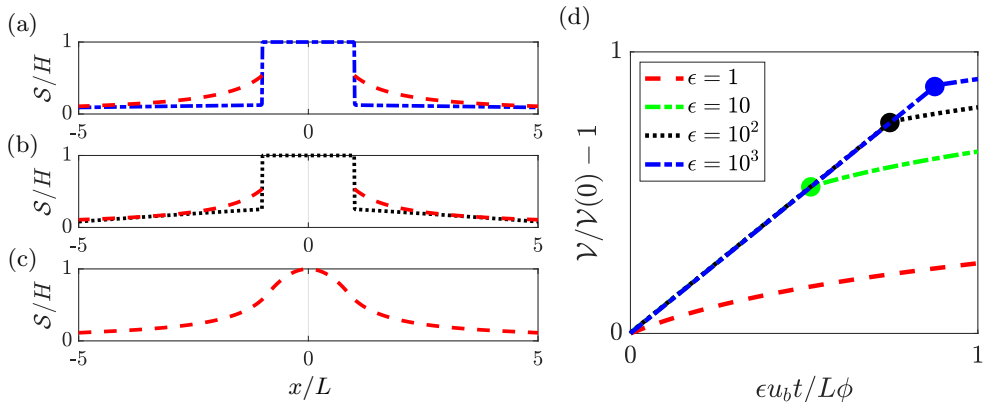


Figure 3: (a,b) Swept shape of the gravity current $\mathcal{S}(x)$ in the case of $\epsilon = 10^{-3}$ and 10^{-2} . (c) Self-similar isotropic case $\epsilon = 1$ (note the modified initial conditions). (d) Evolution of the swept volume $\mathcal{V}(t)$ for each of these cases (note that time is stretched by a factor ϵ). Transition times t^* are indicated with coloured dots.

which is only valid for $x \gg L$. Hence, the swept volume (up to a constant C) is

$$\mathcal{V}(t) = \frac{2HL}{3^{1/2}} \log x_N(t) + C, \quad (3.5)$$

which clearly diverges like $\sim \log t$ as $t \rightarrow \infty$. The constant of integration is found by equating (3.1) and (3.5) at the transition time t^* . Hence, the late time behaviour of the swept volume is given by

$$\mathcal{V}(t) = 2HL + 2\epsilon u_b L t^* + \frac{2HL}{3^{1/2}} \log \left(\frac{t}{t^*} \right)^{1/3}. \quad (3.6)$$

In figure 3a,b,d, the swept shape $\mathcal{S}(x)$ and swept volume $\mathcal{V}(t)$ are plotted for different values of the anisotropy ϵ . For $\epsilon \ll 1$, the anisotropy restricts the swept shape (for $x > L$) to finger-like regions near the base of the current. The maximum thickness of the fingers is set by H^* (2.34), which scales like $H^* \sim \epsilon^{1/3}$. Furthermore, anisotropy delays the transition time according to $t^* \sim \epsilon^{-1}$, whilst for $t \ll t^*$ the swept volume grows slowly, like $\mathcal{V} \sim \epsilon t$. Note that the kinks at the corners $x = \pm L$ (in \mathcal{S}) and at the transition times $t = t^*$ (in \mathcal{V}) would be smoothed out by second order and intermediate asymptotics. However, these do not affect the overall leading order behaviour displayed here.

For comparison, we also plot the swept shape \mathcal{S} in the isotropic case $\epsilon = 1$ in figure 3c. Since our model only applies for $\epsilon \ll 1$, the initial dynamics involving regions I and II are not relevant for this case. Instead, we set the initial shape as

$$h(x, 0) = H \left[1 - \left(\frac{x}{L} \right)^2 \right], \quad (3.7)$$

which is simply the similarity solution (2.31) (note the initial swept volume is then modified to $\mathcal{V}(0) = 4HL/3$). Since the initial shape satisfies the similarity conditions, this ensures that the solution remains self-similar for all times. The corresponding swept shape $\mathcal{S}(x)$ is plotted with red dashed lines in figure 3a,b, for comparison with the anisotropic cases. Clearly, the classical (isotropic) self-similar solution has the largest swept shape and the fastest growing swept volume of all these cases. In the next section,

we discuss how these results can be applied when modelling contaminant spills and CO₂ sequestration, noting the possible limitations of our model.

4. Discussion and applications

The gravity-driven spreading of a finite volume of fluid in anisotropic porous media differs from the isotropic case since the vertical flow is restricted by the permeability $k_V \ll k_H$. In the initial dynamics the bulk of the flow descends slowly with a boundary layer near the impermeable base that diverts the flow into thin finger-like regions growing slowly in the lateral direction. This partition of the flow into bulk and finger regions reduces the swept volume of the gravity current compared to the isotropic case. This indicates that released volumes in anisotropic aquifers contact a smaller fraction of the available pore space. Hence, the spread of a contaminant in an anisotropic aquifer may be easier to contain since the contacted volume is reduced. By contrast, in the case of CO₂ sequestration, where the aim is to trap as much CO₂ in the pore space as possible, isotropic aquifers may have better potential in terms of residual trapping (which is a function of the contacted volume of pore space), though this ignores other trapping mechanisms such as dissolution, structural trapping and mineralisation (Krevor *et al.* 2015).

It is important to consider the possible limitations of this model for such realistic scenarios. First and foremost, it must be noted that the anisotropic permeability values k_H , k_V , are upscaled quantities which attempt to capture the macroscopic effect of small-scale heterogeneities on the flow. These upscaled quantities are only a good approximation when the vertical length scale of the flow H is much larger than the heterogeneity length scale (e.g. the width of sedimentary layers) or when the permeable interval is inherently anisotropic due to compaction effects. If this is not the case, more complex flow models are required to treat the spread of fluid beneath and through successive layers (Neufeld & Huppert 2009; Huppert & Neufeld 2014; Hewitt 2022).

Another consideration for the case of CO₂ sequestration is the effect of trapped saturation on the dynamics and spreading of the current. As the current moves, a fraction of its mass is lost to residual trapping due to small scale capillary forces (Krevor *et al.* 2015) and dissolution (MacMinn *et al.* 2011). According to some trapping models (Golding *et al.* 2017) this can arrest the spread of the current altogether. Likewise, the spreading could also be arrested by lateral heterogeneities in the capillary pressure pinning the nose of the gravity current.

Whilst the conclusion of this study is that anisotropy reduces the swept volume of the gravity current, this doesn't take into account the enhanced trapping potential due to changes in the capillary pressure across heterogeneities, also known as capillary heterogeneity trapping (Harris *et al.* 2021). Specifically, during the imbibition cycle small-scale capillary forces induce a build-up of saturation beneath each sedimentary layer that can account for as much as 14% of the overall trapped saturation. Hence, the optimum anisotropy will no doubt strike a balance between the trapping associated with these heterogeneities and the reduction in swept volume that they induce.

It is also worth mentioning the flow of the ambient fluid, which we have so far ignored for this study. In particular, wherever there are sharp changes in the interface shape, this may be associated with non-negligible displacement of the local ambient fluid, such that the dynamic boundary condition (2.7) cannot be applied. Likewise, in the case where there is a viscosity contrast between the released and ambient fluids (e.g. CO₂ is typically 30 times more viscous than brine), this can modify the shape of the current (Pegler *et al.*

2014) and cause fingering instabilities (Saffman & Taylor 1958). In both of these cases a full numerical model would be necessary to resolve such flow details.

REFERENCES

- BALL, TV, HUPPERT, HE, LISTER, JR & NEUFELD, JA 2017 The relaxation time for viscous and porous gravity currents following a change in flux. *J. Fluid Mech.* **821**, 330–342.
- BARENBLATT, GI 1952 On some unsteady motions of a fluid and a gas in a porous medium. *Prikl. Mat. Makh.* **16**, 67–78.
- BEAR, J & CHENG, AHD 2010 *Modeling groundwater flow and contaminant transport*. Springer.
- BENHAM, GP 2022 The near-field shape and stability of a porous plume. *arXiv preprint arXiv:2204.13510* .
- BENHAM, GP, NEUFELD, JA & WOODS, AW 2022 Axisymmetric gravity currents in anisotropic porous media. *J. Fluid Mech.* **952**, A23.
- CORBETT, PWM & JENSEN, JL 1992 Variation of reservoir statistics according to sample spacing and measurement type for some intervals in the lower brent group. *The Log Analyst* **33** (01).
- GILMORE, KA, SAHU, CK, BENHAM, GP, NEUFELD, JA & BICKLE, MJ 2022 Leakage dynamics of fault zones: Experimental and analytical study with application to CO₂ storage. *J. Fluid Mech.* **931**.
- GOLDING, MJ, HUPPERT, HE & NEUFELD, JA 2017 Two-phase gravity currents resulting from the release of a fixed volume of fluid in a porous medium. *J. Fluid Mech.* **832**, 550–577.
- GUÉRIN, A, DEVAUCHELLE, O & LAJEUNESSE, E 2014 Response of a laboratory aquifer to rainfall. *J. Fluid Mech.* **759**.
- HARRIS, C, JACKSON, SJ, BENHAM, GP, KREVER, S & MUGGERIDGE, AH 2021 The impact of heterogeneity on the capillary trapping of CO₂ in the Captain Sandstone. *Int. J. Greenh. Gas Con.* **112**, 103511.
- HESSE, MA, ORR, FM & TCHELEPI, HA 2008 Gravity currents with residual trapping. *J. Fluid Mech.* **611**, 35–60.
- HESSE, MA, TCHELEPI, HA, CANTWEL, BJ & ORR, FM 2007 Gravity currents in horizontal porous layers: transition from early to late self-similarity. *J. Fluid Mech.* **577**, 363–383.
- HEWITT, DR 2022 Evolution of convection in a layered porous medium. *J. Fluid Mech.* **941**.
- HUPPERT, HE & NEUFELD, JA 2014 The fluid mechanics of carbon dioxide sequestration. *Ann. Rev. Fluid Mech.* **46**, 255–272.
- HUPPERT, HE & WOODS, AW 1995 Gravity-driven flows in porous layers. *J. Fluid Mech.* **292**, 55–69.
- JACKSON, SJ & KREVER, S 2020 Small-scale capillary heterogeneity linked to rapid plume migration during CO₂ storage. *Geophys. Res. Lett.* p. e2020GL088616.
- KOCHINA, IN, MIKHAILOV, NN & FILINOV, MV 1983 Groundwater mound damping. *Int. J. Eng. Sci.* **21** (4), 413–421.
- KREVER, S, BLUNT, MJ, BENSON, SM, PENTLAND, CH, REYNOLDS, C, AL-MENHALI, A & NIU, B 2015 Capillary trapping for geologic carbon dioxide storage—from pore scale physics to field scale implications. *Int. J. Greenh. Gas Con.* **40**, 221–237.
- MACMINN, CW, SZULCZEWSKI, ML & JUANES, R 2011 CO₂ migration in saline aquifers. Part 2. Capillary and solubility trapping. *J. Fluid Mech.* **688**, 321–351.
- NEUFELD, JA & HUPPERT, HE 2009 Modelling carbon dioxide sequestration in layered strata. *J. Fluid Mech.* **625**, 353–370.
- PEGLER, SS, HUPPERT, HE & NEUFELD, JA 2014 Fluid injection into a confined porous layer. *J. Fluid Mech.* **745**, 592–620.
- SAFFMAN, PG & TAYLOR, GI 1958 The penetration of a fluid into a porous medium or Hele-Shaw cell containing a more viscous liquid. *Proc. R. Soc. A.* **245** (1242), 312–329.
- SOLTANIAN, MR, AMOOIE, MA, DAI, Z, COLE, D & MOORTGAT, J 2016 Critical dynamics of gravito-convective mixing in geological carbon sequestration. *Sci. Rep.* **6** (1), 1–13.
- WOODS, AW 2015 *Flow in porous rocks*. Cambridge University Press.